Characterization of Nanostructures at GBs by FEG-TEM and Computational Calculation

Yingda Yu, Dehai Ping, Yuchen Wang, Jianyu Huang,
Douxing Li and Hengqiang Ye

Laboratory of Atomic Imaging of Solids, Institute of Metal Research, Chinese Academy of Sciences, Shenyang 110015, China

(Received: Jan. 30, 1997 Accepted: Feb. 20, 1997)

Abstract

It is recognized that grain boundary structure characterization is essential in order to understand the structure-property relationship of nanocrystalline materials. In most case, nanocrystalline materials have to suffer deformation during compacting or ball milling techniques. Hence a deep and systematic study on deformation mechanism is also necessary. In this paper, characterization of microstructures in nanocrystalline materials synthesized from three different methods, and analyzed by FEG-TEM and computational calculation has been presented.

1. Introduction

Polycrystalline materials with nanometer-sized grains (less than 100 nm), or called nanocrystalline (NC) materials[1] have many potential applications. Recent studies have suggested that NC materials exhibit a variety of novel properties[2,3], such as abnormal thermal expansion, high elastic constant, strengthening fracture stress, high ductility, larger diffusivity etc., which are differing distinctly from those of conventional polycrystalline materials. Since a large portion of the atoms in NC materials resides in grain boundaries (GBs) or interfaces, the structures of these interfaces show significant effects on the properties of NC materials[4-6]. Therefore, an understanding of the atomic structures of GBs is essential in order to clarify the structure-property relationship of NC materials.

So far, the synthesis of NC materials has been carried out most frequently by employing three different kind techniques, which include the inert gas condensation and in situ compacting method (IGCC), the amorphous crystallization method (ACM), and the mechanical alloying (MA)/ball-milling processing (BM, that often refers to the milling of single component powders). Since the amount of atomic displacement during the synthesis depends primarily on the corresponding interatomic potential, the different NC materials synthesized from these three methods are expected to exhibit different atomic structures in their nanocrystalline states. In most case, nanocrystalline materials have to suffer deformation during compacting or ball milling techniques. Hence a deep and systematic study on deformation mechanism is also necessary.

High resolution transmission electron microscopy (HRTEM) nowadays achieves routinely a resolution of slightly better than 0.2 nm. This is sufficient to reveal GB structures of NC materials in particular orientations, i.e. along low-index zone axes. The new generation field emission gun transmission electron microscope (FEG-TEM) allows accurate characterization of the nano-scale microstructure in combination with energy-dispersive X-ray spectroscopy (EDS), electron energy-loss spectroscopy (EELS) and HRTEM on the same TEM, which brings new capabilities to investigate GB structures in NC materials.

In our previous paper[7], the similarity and difference of GB structures in NC materials synthesized by the above three different methods have been studied by HRTEM. The objective of the present paper is to characterize the microstructure in NC, which can not be revealed by HRTEM alone. In a $Ti_{80-x}Nd_xSi_{20}$ alloy made by ACM, EELS nano-scale composition analysis was performed to determine the segregation behavior of the minor element Nd. For a NC Pd materials prepared by IGCC, the atomic structure features of Σ=11 GB and (111) twin boundary are analyzed in detail by means of molecular dynamics computation and image simulation. In an NC Fe-Cu system prepared by MA, EDS nano-scale composition analysis demonstrates

that a supersaturated solid solution has really formed in this immiscible system due to MA.

2. Experimental Procedure

2.1 Specimen Preparation

For ACM sample, a small ingot (~30g) of alloy with the minor rare earth element Nd in $Ti_{80-x}Nd_xSi_{20}$ (x=0.05, 0.1, 0.2, 0.4 at.%) alloy was prepared by arc melting using a tungsten electrode under an argon atmosphere. Rapid liquid quenching was accomplished by using an arc-melting piston and anvil apparatus[8]. The thickness of the splats was in the range of 10-100 μm. The nature of microstructure in each splat was examined by both HRTEM and X-ray diffraction (XRD, Rigaku D/Max-8A diffractometer, Cu K_α radiation). Discs, 3 mm in diameter, were punched out from the as-quenched splats, and then sealed in evacuated quartz tubes for heat treatment.

The NC Pd sample was synthesized by IGCC technique as described in [4]. The chamber for evaporation was first evacuated to an UHV of 7.6×10^{-6} Pa and then filled with high purity helium gas to a pressure of 1 kPa. The Pd crystallites, with an average grain size of 10 nm, were prepared by evaporating the raw Pd material (with a purity of 99.99 wt%) by using a tungsten heater, and collected on a cold finger cooler with liquid nitrogen. The disc-shaped NC Pd bulk samples, 6 mm in diameter and about 100 μm in thickness, were prepared by in situ compacting the Pd crystallites under an uniaxial pressure of 1.5 GPa in a 10^{-6} Pa UHV device.

For MA $Fe_{16}Cu_{84}$ sample, element Fe and Cu with particle size of about 300 mesh were milled in a planetary ball mill in argon atmosphere using steel containers and balls. The ball-to-powder weight ratio was 20:1. The preparation of f.c.c. $Fe_{16}Cu_{84}$ specimen was divided into two steps: firstly, 4.3g Cu and 5.7g Fe powder mixture was milled until the b.c.c. diffraction peaks completely disappeared; then 30g additional Cu powder was added to the original as-MA sample and continued the milling until large agglomerates were produced. The MA specimen was characterized by XRD and HRTEM.

In order to avoid the possible structural change of the thin foil specimen during the HRTEM sample preparation[9], mechanical grinding and ion beam milling were not used for ACM and IGCC samples. These two kinds of HRTEM specimens were prepared directly from the as-prepared NC samples, by twin-jet electropolishing. The HRTEM specimen for MA sample was prepared by mechanical grinding, dimpling, and subsequent ion beam milling of the small agglomerates formed $Fe_{16}Cu_{84}$ during MA.

2.2 Electron Microscopy and Microanalysis

HRTEM experiments were performed using a JEOL 2000EXII HRTEM and a Hitachi HF-2000 FEG TEM operating at an accelerating voltage of 200 kV with interpretable resolution 0.21 nm and 0.24 nm, respectively. The HF-2000 microscope is fitted with Link SuperATW widow EDS detector, and with Gatan 678 Imaging Filter (GIF) system, that enables to carry out the nano-scale composition analysis in the same microscope with a electron beam probe diameter about 1 nm in the microanalysis mode. EELS microanalysis was performed in TEM image mode (i.e. diffraction coupling) with a screen magnification in the range of 60-100 K, and the quantification of the EDS spectra was performed using the Cliff-Lorimer quantitative procedure.

2.3 GB Calculation Method

For the f.c.c. structure, the embedded-atom method (EAM) potential [10] has been used for GB structure calculation in Al and given a better fit between simulated and experimental image[11]. So in the present work, GB models were calculated by using EAM potential to perform relaxation calculation by means of a conjugate gradient minimization technique of molecular dynamics[12]. Periodic boundary conditions are imposed in the directions contained in the boundary plane. Fixed boundary conditions are applied in the normal direction of the interface plane, and allowance is made for possible different rigid body translation of the top grain with respect to the bottom one in order to keep volume unchange. The related computation procedure has been described by Pond and Vitek in [13]. Then the obtained suitable models were used in HRTEM image simulation by the multislice algorithm for comparing with the observed experimental image.

3. Results and Discussion

3.1 Microstructural and Composition Analyses of ACM Ti-Si-Nd Amorphous Alloy

The fully crystallized $Ti_{80-x}Nd_xSi_{20}$ (x=0.05, 0.1, 0.2, 0.4) specimens exhibited the different microstructural features with those of the x≤0.1 specimens. XRD and TEM investigations reveals that only two crystalline phases of Ti_5Si_3 and predominant α-Ti formed in the completely crystallized $Ti_{80-x}Nd_xSi_{20}$ alloys with x≤0.1, and the grains of two phases have distributed homogeneously[14]. While with x≥0.2, the microstructure of the alloys mainly consists of coarse-grained Ti_3Si matrix phase and randomly oriented α-Ti nanocrystalline particles, which embedded in the Ti_3Si grains. TEM observations also show that the overall microstructural features of the x=0.2, 0.4, and 0.8 Nd-containing specimens are similar, hence the experimental results for the x=0.4 Nd-containing specimen will be discussed in detail here.

Fig.1(a) is a typical TEM bright field micrograph of the x=0.4 sample annealed at 570 °C for 1 hr. The enlarged image in Fig.1(b) clearly shows that high density of fine crystallites existed homogeneously in the matrix grains. The coarse matrix grains with the average grain size of about 5 μm as shown in Fig.1(a) was identified as Ti_3Si phase. The corresponding selected area electron diffraction (SAED) pattern along the $[001]_{Ti3Si}$ zone axis is shown in Fig.1(c). Fig.1(d) shows the SAED pattern taken from the area shown in Fig.1(b). In order to clearly index the SAED pattern of the fine particles in the selected area, the low index zone axes of the Ti_3Si matrix phase was titled off the incident electron beam direction. The diffraction peaks of the hexagonal α-Ti phase could be clearly observed in the figure and no evidence for the presence of rare earth compounds was detected from Fig.1(d). Ti_5Si grains were also observed sometimes but few encountered during TEM observation.

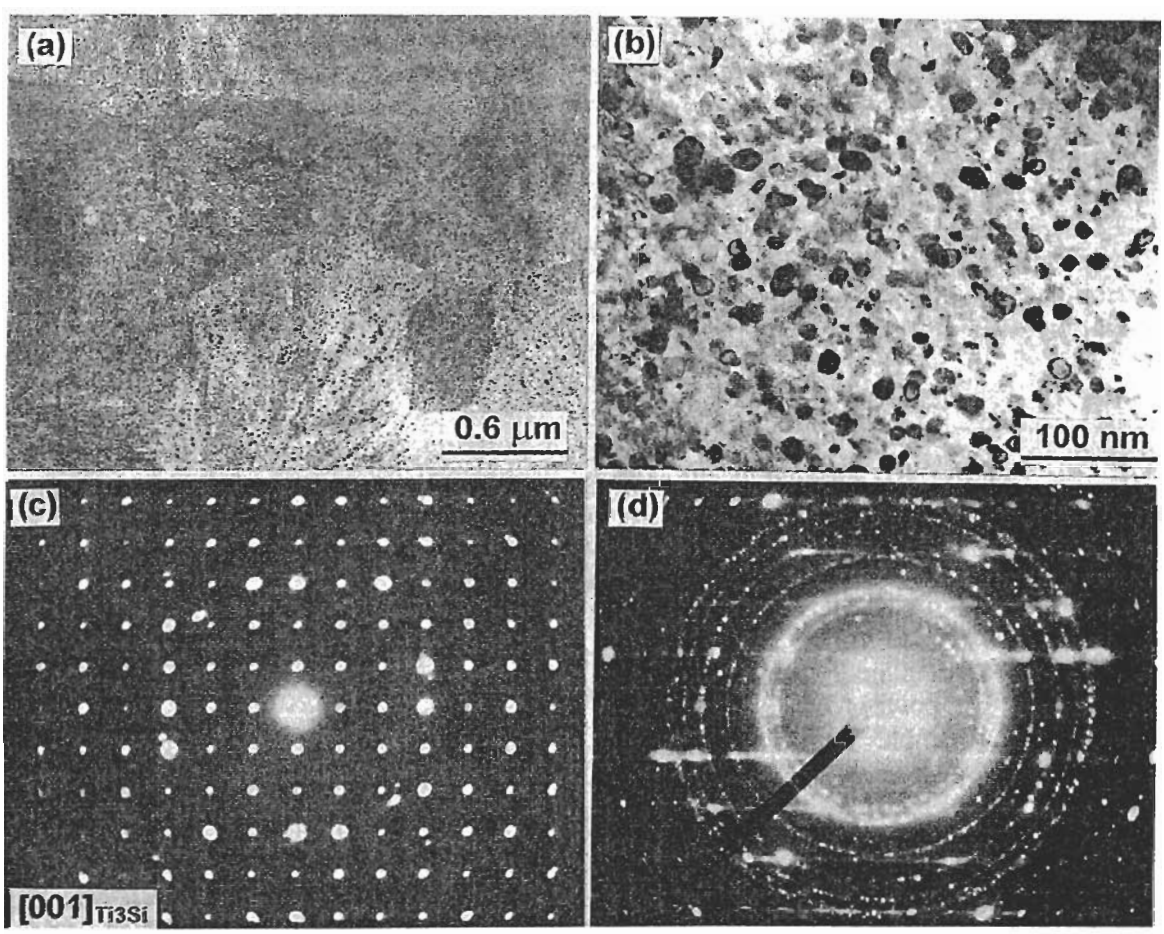

Fig. 1 TEM results of the $Ti_{80-x}Nd_xSi_{20}$ (x=0.4) specimen annealed at 570 °C for 1 hr prepared by ACM. (a) low magnification bright field micrograph showing the typical morphology of the coarse-grained Ti_3Si matrix phase, (b) high magnification bright field micrograph showing the fine α-Ti particles embedded in the matrix phase, (c) SAED pattern from the $[001]_{Ti3Si}$ zone axis of (a), and (d) SAED pattern of (b) showing the diffraction rings of hexagonal α-Ti.

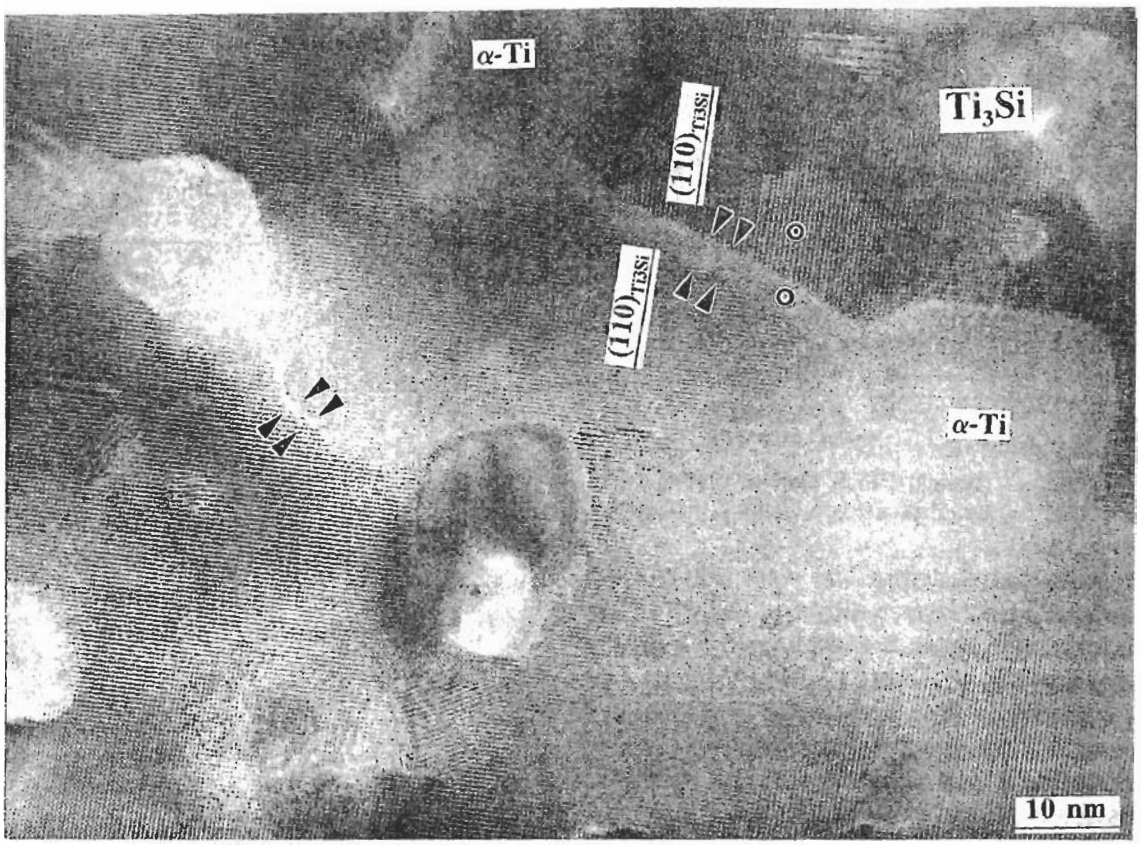

Fig. 2 HRTEM micrograph showing an amorphous phase boundary exists in the $Ti_{80-x}Nd_xSi_{20}$ (x=0.4) specimen annealed at 570 °C for 1 hr.

Fig.2 shows the HRTEM image observed along the $[001]_{Ti3Si}$ zone axis in the same specimen, where Ti_3Si GBs are marked by the arrows in the figure. Residual amorphous structure in the region of GB can be observed as marked by the double arrows, and it could also be found that a small orientation difference exists between the $(110)_{Ti3Si}$ lattice planes of these two grains beside the amorphous phase boundary. It could be expected that a Ti_3Si subgrain boundary would form in this region as the annealing time is increasing. It can also be seen that the grains of the Ti_3Si phase consist of many sub-grains with scale about 40 nm, and small α-Ti particles with dimension about 10 nm.

Nano-scale composition EELS analyses indicated that the minor Nd element has segregated to the amorphous boundary. Fig.3 shows the typical EELS spectra acquired from the Ti_3Si matrix phase (a), and (b) from the amorphous boundary region as marked by the double arrows with a small circle in Fig.2. Nd M4,5 edges can be obviously seen from the spectrum acquired from the amorphous phase boundary in Fig.2. Unlike the standard liquid solidification in alloy, α-Ti particles are not easily movable in the amorphous matrix during the growth of Ti_3Si matrix grain, thus the Ti_3Si grains will grow around the small α-Ti particles, and then encounter with each other. Owing to the irregular shape of the particles and the many particles existing in front of the growing Ti_3Si grains, it is hardly to keep the formation of a flat straight boundary in hardly generated. Since the EELS microanalysis reveals that the minor Nd has segregated to disorder boundary region, this could conclude that the enrichment of Nd in the residual amorphous region should be the reason for further slowing the growth of the NC materials prepared using AMC method.

3.2 Computational analysis of Σ=11 GB and gilding at (111) twin plane of NC Pd

The most direct information regarding the atomic structures of GBs can be obtained from the HRTEM observation when both the GB plane and the low index zone axes of the neighboring grains are parallel to the incident electron beam. The HRTEM observations indicated that NC Pd prepared by IGCC method consists of small crystallites with different crystallographic orientations separated by GBs.

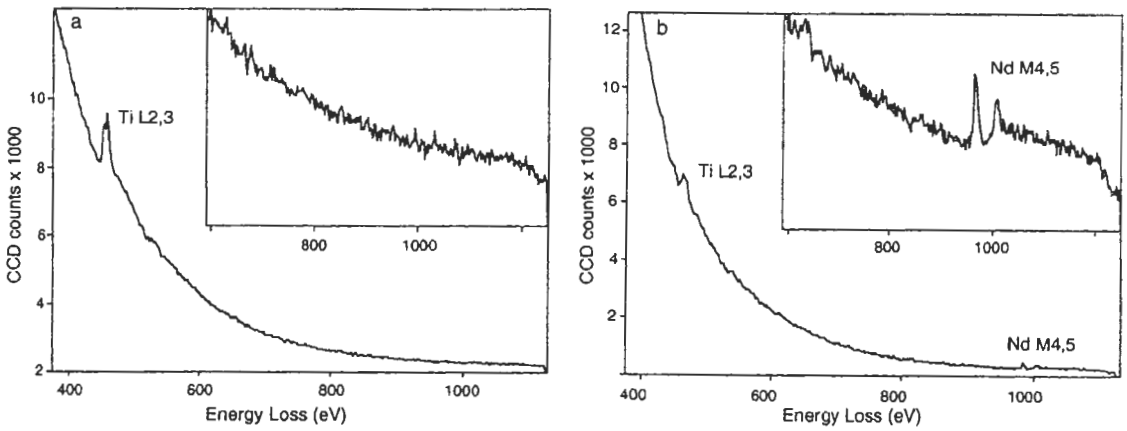

Fig. 3 Typical EELS spectra of the Ti_3Si matrix phase (a) and the amorphous phase boundary (b) acquired using a Gatan GIF system from the region in Fig.2.

The grain-size distributions were determined by XRD and TEM observations. The average grain size obtained from measuring more than 300 grains was about 10 nm[15,16].

Fig.4 shows an HRTEM image of a typical area containing a number of grains and GBs in NC palladium. It can be seen that the most of the GBs have ordered structure, and there are no significant difference between the IGCC NC palladium and coarse grained GBs. However, the GBs are curved due to the extremely small grain size in NC specimens. The lattice fringes near the GBs between grains 1, 4, 5, 6 and 7 in Fig.4 are slightly distorted, which indicate the presence of local strain in the GB regions. Somewhat imperfect or disordered GB regions have also been observed. The GB, indicated by 'd', between grains 1, 2 and 3 in Fig.4 is different from that of the GBs mentioned above, showing that there is disorder at the GB region. No apparent lattice fringes can be seen from the area with brighter contrast than the interior crystallites, indicated by 'v' in Fig.4; the contrast in the area remains unchanged at various defocus. It is suggested that the area is a nano-void formed during the compacting process.

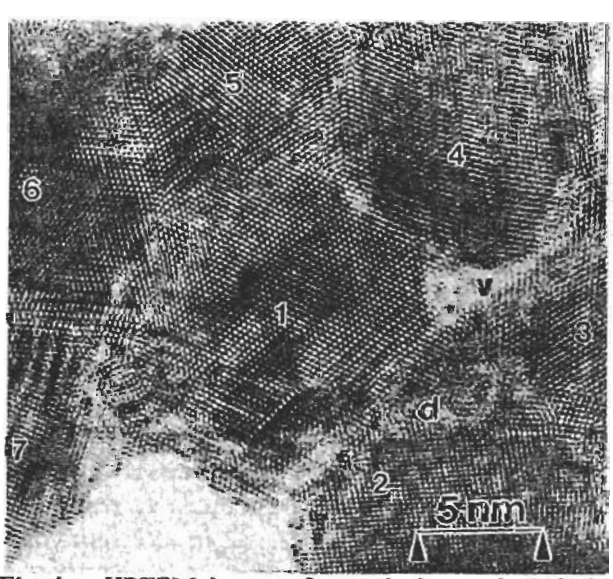

Fig. 4 HRTEM image of a typical area in NC Pd prepared by IGCC method.

A high magnification HRTEM image with a (113) tilt boundary and a (111) twin in this NC Pd, viewed along [1$\bar{1}$0], is shown in Fig.5(a), where the interfaces are marked by the arrows. The closest distance of Pd atoms on the (1$\bar{1}$0) projected plane is about 0.24nm, that is within the resolution of the used electron microscope. Two enlarged segments containing (113) boundary and (111) twin are shown in Figs. 5(b) and (c), respectively. From Fig.5(b), it can be found that the (113) interfacial plane is flat and the contrast of the bright spots at the interface are the same as those in the matrix. However, some distortions can be seen near twin plane as shown in Fig.5(c). By measuring of bright spot positions, it can be found that there are two possible slips. One is that the upper grain translates to the right about 1/5 period vector (henceforth the period vector referred to as T_{twin}) with respect to the lower grain, another shift is to the left about $(3/10)T_{twin}$.

For the Σ=11/[1 $\bar{1}$0] boundary, the initial unrelaxed configuration is constructed, where the atom positions are projected on to the (1$\bar{1}$0) plane. By relaxation computation by using 4422 atom supercell, the final relaxed configuration of (113) GB was obtained with the corresponding GB energy as 360 mJ/m^2. By means of the image simulation of the perfect Pd in the same orientation, the actual imaging conditions of the observed GB image could be

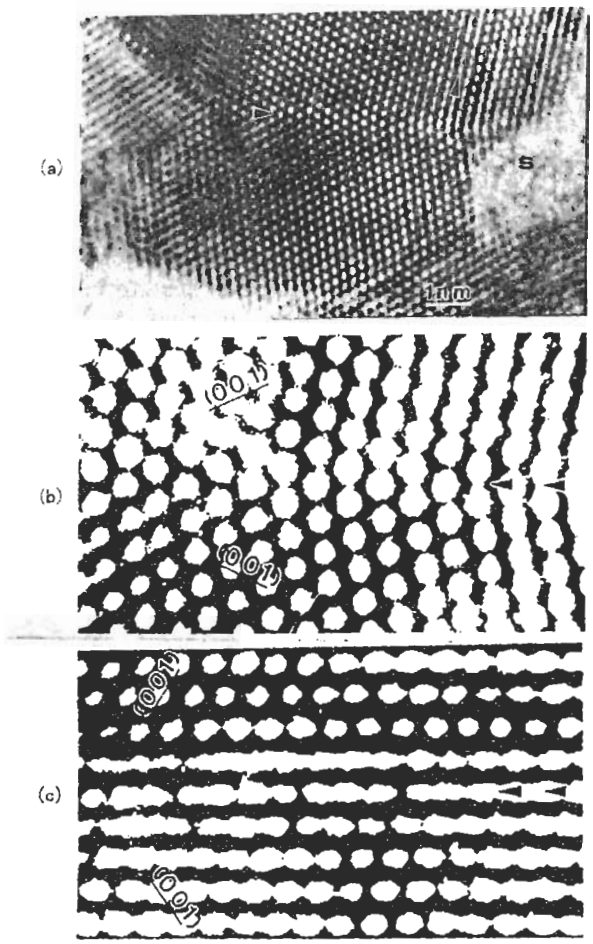

Fig. 5 (a) HRTEM image of the NC Pd with a (113) GB and a (111) twin, where the interfaces are indicated by arrows, (b) an enlarged segment of the (113) GB, and (c) an enlarged segment of the (111) twin.

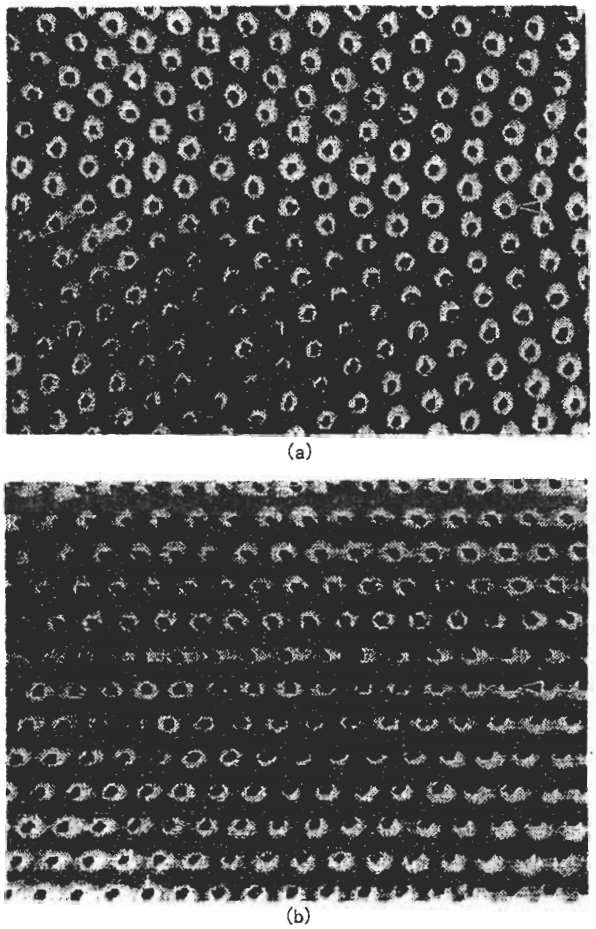

Fig. 6 The superimpose of images between the simulated and experimental images of the (113) GB (a), and (111) twin (b), where the bright spots come from experimental images and the black dots from calculated images.

determined. Then by using the obtained final relaxed configuration with the determined imaging condition, the final simulated image could be retrieved. To make comparison between the final simulated image with the experimental observed one more quantitative, a direct overlay of the simulated and experimental images is shown in Fig.6(a). For producing this superimposed image, the simulated image was reversed in contrast (small black spots in Fig.6(a)), and then superimposed transparently onto the experimental image (large white spots). In the overlaid black spot image, the contrast level was enhanced in order to produce a smaller spot size that makes the experimental white-spot image visible. The detailed computational and simulated procedures are described in [17]. For the case of the deformed (111) twin boundary, the similar procedures were used. The final relaxed configuration with about $(1/5)T_{twin}$ translation along $[1\bar{1}\bar{1}]$ and GB energy 145 mJ/m^2 are determined as the most suitable one through comparing the GB energies of the different configurations. The corresponding resulted superimposed image is shown in Fig.6(b).

From better match as shown in Figs. 6(a) and (b), it can be concluded that the final relaxed models have the realistic configurations, which are also the typical structures of coarser-GB. The deformed (111) twin plane similar to the final relaxed configuration with about $(1/5)T_{twin}$ translation along [111] was coincided with that in ball milled Cu as well[18].

It is a general knowledge that there are large stress in inter-grain region as marked by letter 'S' in Fig.5(a) due to the serious misfit among grains. These stress could be released by located atom position changes or GB glide. In consideration of the deformed region, the curves of GB energy vs. rigid displacement between the upper and lower ones (interfacial planes belong to lower grains) are calculated as

shown in Fig.7, where the above two resulted configurations are regarded as the initial models, and the GB energies were calculated according to the every rigid displacement possibilities. It should be noted that the curves in the figure only show the relationship between the GB energy and displacement qualitatively rather than quantitatively. In Fig.7, the curves with 'A' and 'B' labels indicated the cases for (111) twin and Σ=11 GB, respectively. From the calculated curves of GB energies vs. rigid displacement, it is found that the curve A is highly asymmetrical about the grid displacement. This implies that the displacement of (111) twin along [11 $\bar{1}$] is difficult to released the stress, but that along [$\bar{1}\bar{1}$1] is easier. It is reasonable to conclude that the observed Σ=11 GB is a stable one, and difficult to release stress by any atomic rearrangement, while the (111) twin, however, is easy to release the stress by gilding deformation along the [$\bar{1}\bar{1}$1] direction.

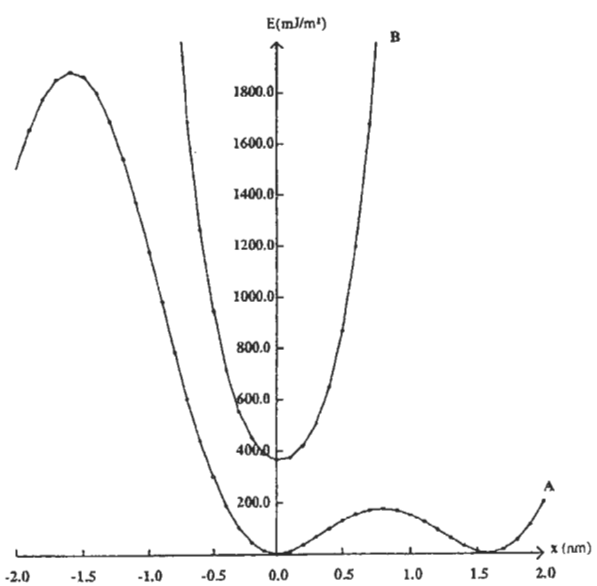

Fig. 7 The calculation curves of GB energy vs. rigid shift, where the letters A and B indicated the relationships for the (111) twin and the Σ=11 (113) GB, respectively.

3.3 Microstructural and composition analyses of MA Fe-Cu system

The previous research on the MA Fe-Cu system[19-20] reveals that the miscibility of Fe in f.c.c.-Cu can be greatly enhanced through MA. Fig.8 shows the TEM micrographs corresponding to MA $Fe_{16}Cu_{84}$ specimen. The SAED patterns of Fig.8(c) exhibits only the characteristic f.c.c. phase, which agrees with the XRD result[20]. From the bright and dark field images shown in Figs. 8(a) and (b), it can be seen that the grain size is relatively homogeneous. The average grain size is in the range of about 10-50 nm. HRTEM image containing a number of grains and GBs is shown in Fig.9. These grains tend to be flattened and atomic layered structures are developed. Even the diffraction peak from the b.c.c. phase has completely disappeared in the SAED patterns of Fig.8(c), small Fe domains

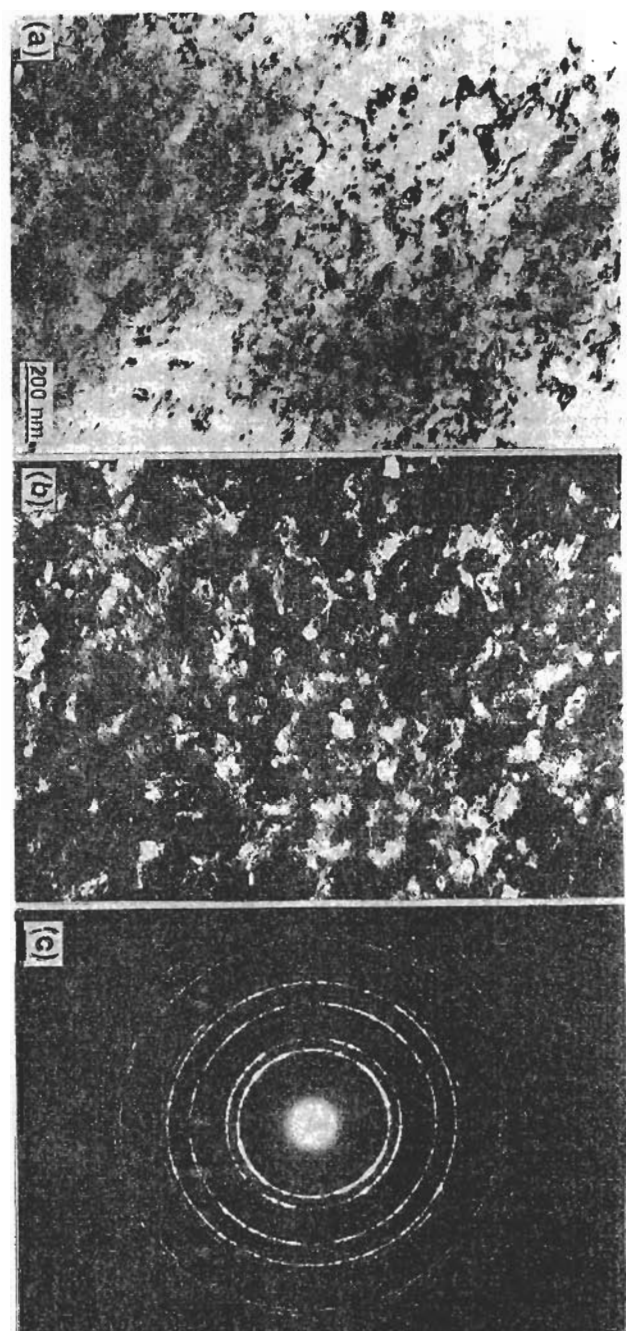

Fig. 8 TEM micrographs of specimen $Fe_{16}Cu_{84}$ specimen. (a) bright field image, (b) dark field images, and (c) corresponding SAED patterns.

can still be detected in the HRTEM image shown in Fig.9, as indicated by a circle.

The nano-scale composition of both the interior grains and the GBs of MA $Fe_{16}Cu_{84}$ was analyzed by EDS. Twenty-three different grains and 18 different GBs in this specimen were randomly selected[20]. Typical EDS spectra from the interior grains and the GBs are shown in Figs 10(a) and (b), respectively. The overall results show that the average Fe contents (about 16%) in both the interior grains and the GBs are very close to the designed composition (16%). The slightly higher Fe content should be due to the Fe contamination from the vials and balls. It can also be found that the Fe contents are rather inhomogeneous, which infers that the mixing of Cu and Fe during MA is far from homogeneous at the atomic level. The higher Fe content

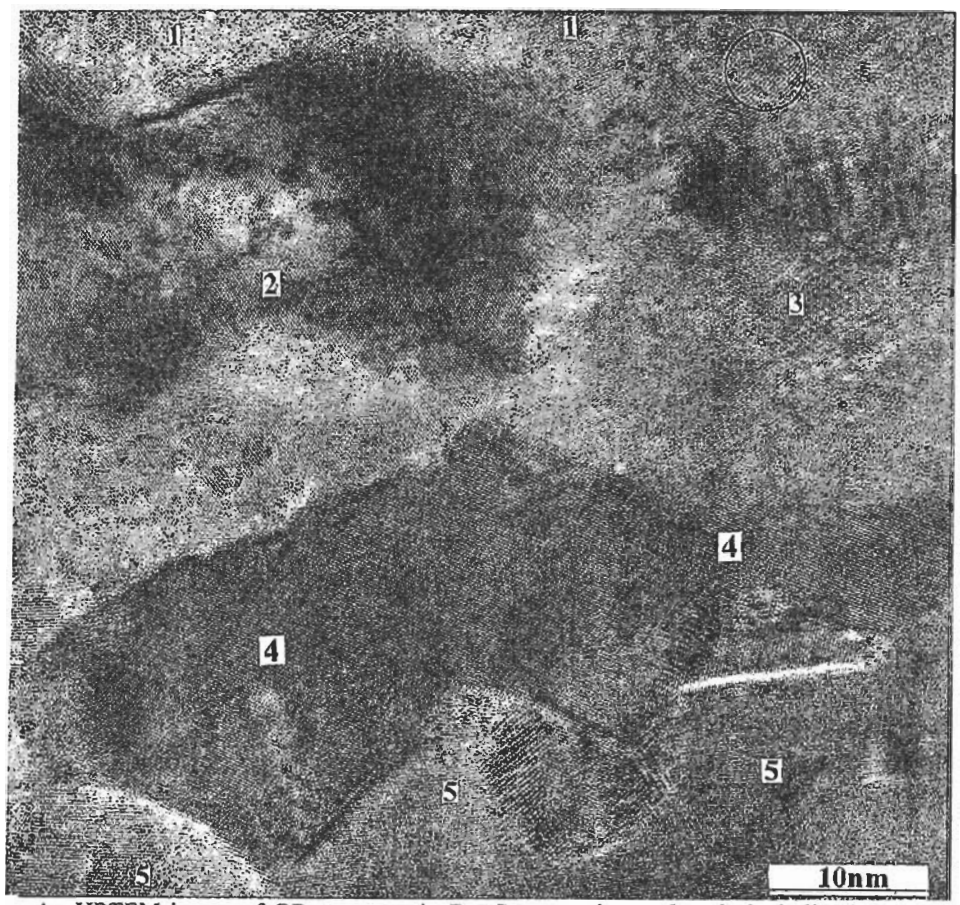

Fig. 9 An HRTEM image of GB structure in $Fe_{16}Cu_{84}$ specimen, the circle indicating a small b.c.c. grain, '1-5' denoting the number of grains.

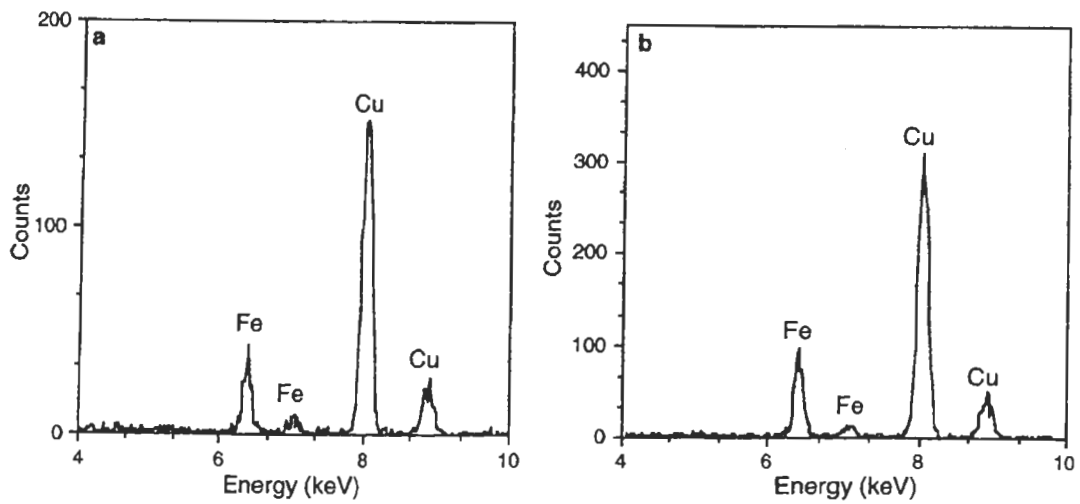

Fig. 10 EDS spectra from MA $Fe_{16}Cu_{84}$ specimen. (a) in the interior grains, and (b) in the GBs.

(>50%) may be due to the undissolved Fe domains inserted into the interior of grains or embedded in the GBs. This is indeed observed in the HRTEM image as shown in Fig.9. Generally the smaller the grain size, the higher the Fe content. However, in most cases the Fe content falls in the range of about 5% to 20%, thus proving that a supersaturated solid solution has really formed in this immiscible system due to MA.

Although MA in Fe-Cu system has been performed by many researchers, whether true alloying has occurred has not been confirmed until now. Because the occurrence of a single fcc Bragg pattern can not be taken as definite evidence for a solid solution on atomic level. This has been demonstrated by XRD investigations on Co/Cu multi-layers[21] and on decomposed Co-Cu solid solutions[22]. Although these materials consist of separate f.c.c. Cu and f.c.c. Co regions they exhibit a diffraction pattern which can hardly be distinguished from the XRD of a solid solution having the same overall composition, if the Cu and Co regions are coherent and their size is smaller than about 5-8 nm. Therefore Bragg peaks of an f.c.c. phase can not be used as proof for the formation a homogeneous solid solution during MA. On the other hand, nano-scale EDS result shows that the average Fe contents in the interior of most Cu grains are close to the designed composition, which is certainly direct evidence for the formation of an atomic level mixing Fe-Cu solid solutions, although the mixing is inhomogeneous. Nanocrystalline structure and fast diffusion may be responsible for the formation of solid solution in immiscible systems with positive enthalpy of mixing. As a result of the small grain size and the formation of defects (especially GBs and interface boundaries), the enthalpy of two phase dispersed mixture may be higher than that of a non-equilibrium solid solution.

4. Summary remark

The GBs and interfacial structures are not only important for understanding a variety of novel properties in NC materials, but also put forward a challenge for characterization technique of materials science. HRTEM, undoubtedly, is a powerful tool to reveal NC structure at the atomic scale with advantage of intuition. The observations of subgrains in the Ti_3Si phase and small α-Ti particles with dimension about 10 nm in ACM Ti-Si-Nd amorphous alloy, as well as the undissolved Fe domains in an apparently complete Cu-Fe solid solution, are the good example to illustrate the merit of HRTEM. Nevertheless more information could be extracted by combination of nano-scale composition analysis by using FEG-TEM for Nd segregation on the GBs of NC Ti-Si-Nd alloy and inhomogeneous distribution of the Fe atoms in Cu-Fe supersaturated solid solution. Moreover, an energy relaxation computation might make the HRTEM images more reliable, such as the reasonable interpretation for the asymmetric Σ3 (111) twin boundary in NC Pd.

Acknowledgmen

Project supported by National Natural Science Foundation of China (NNSFC) and Committee of Science and Technology of Liaoning Province (CSTL), which were gratefully acknowledged.

References

1. H. Gleiter & P. Marquardt, Z. Metallkunde 75, 163(1984).
2. A.H. Chokshi, A. Rosen, J. Karch & H. Gleiter, Scripta Metall. 23, 1679(1989).
3. K. Lu, W.D. Wei & J.T. Wang, Scripta Metall. 24, 2319(1990).
4. R. Birringer, U. Herr & H. Gleiter, Suppl. Trans. Jpn. Inst. Met. 27, 43(1986).
5. H. Gleiter, Prog. Mater. Sci. 33, 223(1989).
6. R.W.Siegel, MRS Bull. 15(10), 60(1990).
7. H.Q. Ye, D.H. Ping, D.X. Li, J.Y. Huang & Y.K. Wu, Proc. Microscopy and Microanalysis 1995, ed. by G.W. Bailey et al. (Jones & Begell Publishing, 1995) p.192.
8. M. Ohring & A. Haldipur, Rev. Scient. Instrum. 42, 530(1971).
9. D.H. Ping, PhD Thesis, Institute of Metal Research, 1995.
10. M.S. Daw, & M.I. Baskas, Phys. Rev. B 29, 6443(1984).
11. U. Dahmen, C.J.D. Hetherington, M.A. O'Keefe, K.H. Westmacott, M.J. Mills, M.S. Daw & V. Vitek, Phil. Mag. Lett. 62, 327(1990).
12. A.P. Sutton, & V. Vitek, Phil. Trans. Roy. Soc. (London) A 309, 1(1983).
13. R.C. Pond, & V. Vitek, Proc. Roy. Soc. A 357, 453 (1977).
14. D.H. Ping, G.P. Li, Y.G. Wang, Y.D. Yu, D.X. Li & H.Q. Ye, Mater. Lett. 24, 121(1995).

15. D.X. Li, D.H. Ping, H.Q. Ye, X.Y. Qin & X.J. Wu, Mater. Lett. 18, 29(1993).
16. D.H. Ping, D.X. Li & H.Q. Ye, J. Mater. Sci. Lett. 14, 1536(1995).
17. Y.C. Wang, D.H. Ping, S.Q. Wang, D.X. Li & H.Q. Ye, Phil. Mag. Lett., submitted.
18. J.Y. Huang, Y.K. Wu & H.Q. Ye, Acta Mater. 44, 1211(1996).
19. J.Y. Huang, Y.D. Yu, Y.K. Wu & H.Q. Ye, J. Mater. Res. 11, 2717(1996).
20. J.Y. Huang, Y.D. Yu, Y.K. Wu, D.X. Li & H.Q. Ye, Acta Mater. 45, 13(1997).
21. C. Gente, M. Oehring & E. Bormann, Phys. Rev. B48, 13244(1993)
22. C. Michaelsen, Phil. Mag. 72, 813(1995).